A semiconducting hybrid of RhO$_x$/GaN@InGaN for simultaneous activation of methane and water toward syngas by photocatalysis

Dongke Li[a,b,12], Zewen Wu[c,1], Yixin Li[a,1], Xiaoxing Fan [ID][b], S.M. Najib Hasan[d], Shamsul Arafin [ID][d], Md Afjalur Rahman[e], Jinglin Li[a], Zhouzhou Wang [ID][a], Tianqi Yu[a], Xianghua Kong[c,*], Lei Zhu[a], Sharif Md. Sadaf[e,*] and Baowen Zhou [ID][a,*]

[a]Key Laboratory for Power Machinery and Engineering of Ministry of Education, Research Center for Renewable Synthetic Fuel, School of Mechanical Engineering, Shanghai Jiao Tong University, 800 Dongchuan Road, Shanghai 200240, China
[b]School of Physics, Liaoning University, No. 66 Chongshan Middle Road, Huanggu District, Shenyang City 110036, Liaoning Province, China
[c]College of Physics and Optoelectronic Engineering, Shenzhen University, 3688 Nanhai Avenue, Nanshan District, Shenzhen 518061, China
[d]Electrical and Computer Engineering, The Ohio State University, Columbus, OH 43210, USA
[e]Centre Energie, Matériaux et Télécommunications, Institut National de la Recherche Scientifique (INRS)-Université du Québec, 1650 Boulevard Lionel-Boulet, Varennes, Quebec J3X1S2, Canada
*To whom correspondence should be addressed: Email: kongxianghuaphysics@szu.edu.cn; sharif.sadaf@inrs.ca; zhoubw@sjtu.edu.cn
[1]D.L., Z.W., and Y.L. contributed equally to this work.
[2]D.L. is a visiting student in Shanghai Jiao Tong University from Liao Ning University.
Edited By: Levi Thompson

Abstract

Prior to the eventual arrival of carbon neutrality, solar-driven syngas production from methane steam reforming presents a promising approach to produce transportation fuels and chemicals. Simultaneous activation of the two reactants, i.e. methane and water, with notable geometric and polar discrepancy is at the crux of this important subject yet greatly challenging. This work explores an exceptional semiconducting hybrid of RhO$_x$/GaN@InGaN nanowires for overcoming this critical challenge to achieve efficient syngas generation from methane steam reforming by photocatalysis. By coordinating density functional theoretical calculations and microscopic characterizations, with in situ spectroscopic measurements, it is found that the multifunctional RhO$_x$/GaN interface is effective for simultaneously activating both CH$_4$ and H$_2$O by stretching the C–H and O–H bonds because of its unique Lewis acid/base attribute. With the aid of energetic charge carriers, the stretched C–H and O–H bonds of reactants are favorably cleaved, resulting in the key intermediates, i.e. *CH$_3$, *OH, and *H, to sit on Rh sites, Rh sites, and N sites, respectively. Syngas is subsequently produced via energetically favored pathway without additional energy inputs except for light. As a result, a benchmarking syngas formation rate of 8.1 mol·g$_{cat}^{-1}$·h^{-1} is achieved with varied H$_2$/CO ratios from 2.4 to 0.8 under concentrated light illumination of 6.3 W·cm^{-2}, enabling the achievement of a superior turnover number of 10,493 mol syngas per mol Rh species over 300 min of long-term operation. This work presents a promising strategy for green syngas production from methane steam reforming by utilizing unlimited solar energy.

Significance Statement

As crude oil dwindles, methane steam reforming toward syngas presents an attractive strategy to power our economy prior to the arrival of carbon neutrality. However, the remarkable geometric and polar discrepancy of CH$_4$ and H$_2$O poses tremendous obstacles for simultaneous activation of CH$_4$ and H$_2$O toward syngas under ambient conditions. In practice, high temperature (700–1000°C) and high pressure (2–3 MPa) are generally required for overcoming the reaction energy barrier. In this work, a semiconducting hybrid of RhO$_x$@GaN/InGaN nanowires is explored for simultaneous activation of CH$_4$ and H$_2$O with notable discrepancy to break the limit of photocatalytic steam reforming toward syngas. This work presents a promising route for next-generation transportation fuels synthesis with the inputs of methane, water, and sunlight.

Introduction

As the petroleum dwindles and shale gas revolution unfolds, solar-driven syngas production from methane steam reforming offers a low-carbon alternative for chemical refineries to produce transportation fuels and chemicals (1–5). Unfortunately, it is highly challenging due to the inert C–H bond, negligible electron affinity, and low polarization of CH$_4$ (6–8). Meanwhile, syngas production from methane steam reforming is, in principle, an endothermic process (CH$_4$ + H$_2$O = 3H$_2$ + CO, ΔH$_{298K}$ = + 206 kJ/mol) (2, 9, 10). Moreover, the geometric and polar difference between

CH_4 and H_2O poses a tremendous obstacle for simultaneously activating these two reactant molecules, making efficient and tunable syngas production substantially challenging. For the present industrial process, high temperature (700–1000°C) and high pressure (>20 bar) (6, 7) are required to stride the high reaction energy barrier, thus suffering from intensive thermal input and severe carbon emission. From the perspective of carbon neutrality, it is very desired to explore a green route to produce syngas production from methane steam reforming, especially if driven by solar energy under mild conditions (11).

Photocatalysis provides a burgeoning means for chemical reactions by activating the reactants with energetic charges. It thus holds a grand promise for breaking the thermodynamic limits of syngas production from methane steam reforming under mild conditions (2, 9, 10). Up to date, a series of laudable endeavors have been conducted to explore suitable photocatalysts by decorating semiconductor materials with various cocatalysts for methane steam reforming, and significant progress has been made (12–14). Nevertheless, producing energetic charges without compromising high optical absorption is difficult. More importantly, there has been lack of an efficient photocatalytic architecture for simultaneously activating CH_4 and H_2O because of their remarkable geometric and polar discrepancy. Thus far, there has been no virtual success in photocatalytic methane steam reforming toward syngas yet. The pursuit of a multifunctional photocatalyst to overcome the critical issues above is thus of scientific and practical importance.

Nanostructured III-nitrides present an appealing semiconductor platform for photocatalysis (15). Such a semiconductor platform enables efficient photon absorption and subsequent energetic charges generation with tailorable redox potentials due to the broadly tunable band structure ranging from 3.4 to 0.65 eV (15–17). Interestingly, wurtzite III-nitrides render a polar- and electronic-tuning surface for coupling with appropriate cocatalysts to simultaneously activate CH_4 and H_2O (17). Meanwhile, the large surface area and 1D geometry of III-nitride nanowires (NWs) are conducive to high accessibility of reactants to catalytic centers (18–20). Of note, among various materials, rhodium (Rh) emerges as an appropriate candidate for methane activation owing to its unique structural and electronic properties (2). According to previous discovery, the electron-deficient state of Rh metal like Rh^+ possesses higher ability to grab electrons of methane and dissociate the C–H bond (21), thus being an ideal candidate to construct a rational photocatalytic architecture by integrating with III-nitride-based platform.

Inspired by the pioneering works above, in this work, we develop a semiconducting hybrid by decorating the attractive platform of vertically aligned GaN/InGaN NWs with ultrafine RhO_x nanoclusters. By correlative theoretical calculations, microscopic characterizations, and in situ spectroscopic measurements, it is discovered that the assembled hybrid of RhO_x/GaN@InGaN NWs is unique for simultaneous activation of both CH_4 and H_2O owing to the Lewis acid/base nature of RhO_x/GaN interface. With the aid of photogenerated energetic charge carriers, the nonpolar CH_4 is facilely split into *CH_3 and H* species while H* and *OH are favorably produced from water splitting. Afterward, *CH_3 and *OH species intend to sit on Rh sites, and H* prefers to be adsorbed on N sites of GaN. The adsorbed active species of *CH_3, *OH, and *H are subsequently evolved toward syngas via energetically favored pathway, thus breaking the thermodynamic limit of syngas production from CH_4 and H_2O under close to ambient conditions. Together, an exceptional syngas activity of 8.11 $mol \cdot g_{cat}^{-1} \cdot h^{-1}$ is achieved under concentrated light irradiation of 6.3 $W \cdot cm^{-2}$

without additional energy inputs. The H_2/CO ratio can be flexibly tailored from 2.4 to 0.8. A superior turnover number of 10,493 mol CO + H_2 per mol Rh are obtained within 3-h operation. This work shows a green avenue for syngas production from methane steam reforming driven by sunlight.

Results and discussion
Theoretical calculations on the multifunctional RhO_x/GaN interface for simultaneous activation of methane and water

As mentioned above, simultaneous activation of both methane and water is crucial for efficient methane steam reforming toward syngas. Thereby, density functional theory (DFT) simulations were conducted to study the adsorption/activation of methane and water over the RhO_x/GaN interface at the molecular level. Firstly, 12 Rh_6O_9/GaN configurations were established (Fig. S1). After fully geometric structure relaxation, the most energetically favorable Rh_6O_9/GaN configuration is confirmed and plotted in Fig. S1a and c, showing the lowest formation energy, i.e. −26 meV/$Å^2$ (Fig. S2). Charge transfer of 0.468 e from GaN surface to Rh_6O_9 cluster is found in this Rh_6O_9/GaN system. To confirm the role of RhO_x and GaN in this work, adsorption characteristics of CH_4, H_2O, and essential intermediates among methane steam reforming over Rh_6O_9/GaN system are then calculated. For CH_4 and H_2O, compared with their original structure information, upon adsorption onto the Rh_6O_9/GaN surface, C–H bonds in CH_4 and O–H bonds in H_2O are all elongated (Table S1) with an average value of 0.022 and 0.056 Å, respectively. These results indicate that both CH_4 and H_2O are activated by the designed Rh_6O_9/GaN system. In this case, the C–H bond and O–H bond can then be readily broken in the presence of photogenerated charges. Moreover, it is found that after C–H bond of CH_4 and O–H bond of H_2O are broken, *CH_3, *OH, and H* prefer to sit on Rh site, Rh site, and N site, respectively. The results of Bader charge analysis revealed that the Rh atom bonded with C atom of *CH_3 and O atom of *OH exhibit electropositive with an amount of 1.098 and 1.252 e, respectively. For the N atom, forming bond with H atom of *H shows electronegative with a value of 1.366 e. Above all, it is rationalized that RhO_x could be served as a Lewis base and GaN functioned as a Lewis acid, which is labeled with symbol "+" and "−," respectively (Fig. 1), demonstrating promising synergistic catalysis for simultaneous C–H bond and O–H bond activation, which is the key step for exceptional steam methane reforming toward syngas.

Fabrication and characterization of the photocatalytic architecture

Inspired by this theoretical discovery, a RhO_x/GaN@InGaN NWs hybrid was developed by combining plasma-assisted molecular beam epitaxy with photodeposition for photocatalytic methane steam reforming. To effectively harvest the incident light and precisely mediate charge carriers and chemical species behavior, multilayer p-doped GaN:Mg/InGaN:Mg NWs were first epitaxially grown on a 3-inch silicon wafer under N-rich atmosphere (Figs. S3 and S4). Detailed procedure of the growth can be referred to our previous work (22). Utilizing the multistacked GaN@InGaN NWs as the scaffold, RhO_x species were deposited to create multifunctional sites to simultaneously activate CH_4 and H_2O. As characterized by scanning electron microscopy (SEM), GaN@InGaN NWs are vertically aligned onto silicon with an average height of about 300 nm, and the diameter is in the range of 30–50 nm (Fig. 2a and Fig. S5). Meanwhile, the large surface area and well-defined
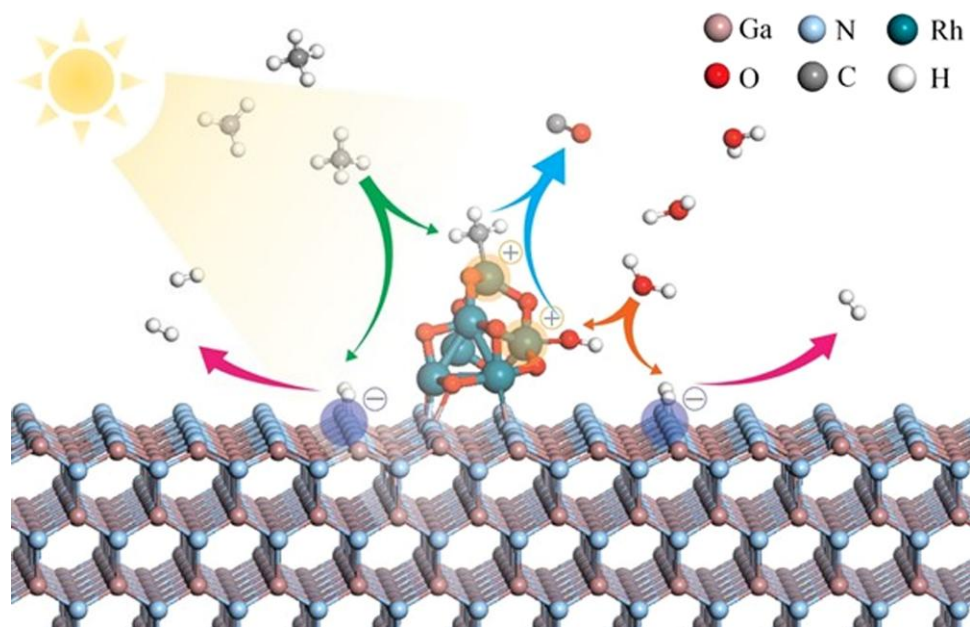
Fig. 1. Schematic for simultaneous adsorption/activation of CH_4 and H_2O by RhO_x/GaN system based on DFT calculations.

1D morphology of GaN@InGaN NWs favor high accessibility of both photons and reactants, thus benefiting the reaction. High-angle annular dark-field scanning transmission electron microscopy characterization in Fig. 2b shows that Rh nanoparticles (Rh NPs) are randomly distributed on the surface of NWs with varied diameters. The lattice spacing of 0.22 and 0.26 nm belongs to the RhO_x and (001) plane of GaN, respectively, which suggests that the growth direction of NWs is the c-axis ([000–1]) (Fig. 2c). The energy-dispersive X-ray spectroscopy mapping further confirmed the success in the anchoring of Rh NPs onto GaN@InGaN NWs/Si (Fig. 2d–g). As estimated by inductively coupled plasma-atomic emission spectroscopy, the loaded content of Rh NPs is as low as $0.34\,\mu mol \cdot cm^{-2}$, which facilitates to achieve high turnover frequency (TOF).

X-ray photoelectron spectroscopy (XPS) measurements were also conducted to study the oxidation states and electronic interaction of the elements in RhO_x/GaN@InGaN NWs (Fig. S6). As shown in Fig. 3, compared with bare GaN@InGaN NWs, the binding energies of Ga 3d, N 1s, and In 3d (Fig. 3a–c) of RhO_x/GaN@InGaN NW exhibit obvious positive shifts, suggesting the electron redistribution from GaN@InGaN NWs platform to the decorated cocatalyst, which is in excellent agreement with DFT calculations above. Of note, the deposited Rh species mainly composed of Rh^{3+} (308.22 eV) (Fig. 3d), suggesting that RhO_x is the major state (23, 24). The bandgap diagram of GaN@InGaN NWs was further determined by combining XPS with photoluminescence (PL) spectroscopy measurements (Figs. S7 and S8). It was noted that the PL intensity decreased after loading of RhO_x (Fig. S8), which indicated that the recombination of photogenerated carriers was suppressed. As shown in Fig. S9, for the NW, the incorporation of In is of benefit to broaden the light absorption by narrowing the bandgap of GaN, thus facilitating the reaction. Overall, a novel RhO_x/GaN@InGaN NWs hybrid is explored, demonstrating unique geometric and optoelectronic properties for simultaneous activation of both methane and water and for providing energetic carriers to break the limits of methane steam reforming toward syngas under ambient conditions, which will be systematically studied next.

Syngas production from CH_4 and H_2O

The experiments were performed in a batch quartz chamber under atmospheric pressure illuminated by a 300-W Xenon lamp without any additional energies input, and the results are shown in Fig. 4. It could be seen that among various noble metals test, Rh species showed the highest activity (Fig. S10), suggesting the superiority of Rh species for decorating GaN@InGaN NWs to catalyze light-driven methane steam reforming toward syngas. By varying the dosage of Rh precursor ($Na_3RhCl_6 \cdot XH_2O$), the influence of the loaded Rh content on the reaction was first investigated. It was observed that in the absence of RhO_x, the multistacked GaN@InGaN NWs were nearly inactive for syngas production because there was lack of catalytic sites (25, 26). In stark contrast, the decoration of RhO_x species affected the performance of methane steam reforming remarkably (Fig. 4a). By increasing the dosage of Rh precursor, the activity of syngas was increased considerably due to the enriched active sites and peaked at a superior rate of $6.5\,mol \cdot g_{cat}^{-1} \cdot h^{-1}$ with a syngas selectivity of 91.2% at an appropriate Rh content of $0.34\,\mu mol \cdot cm^{-2}$. However, the activity of both CO and H_2 dramatically declined to 1.51 and $3.17\,mol \cdot g_{cat}^{-1} \cdot h^{-1}$, respectively, when Rh was overloaded. It is likely attributed to the excessive agglomeration of Rh NPs, which can be validated by TEM characterizations (Fig. S11). Correspondingly, TOF of $CO + H_2$, a key descriptor of catalytic activity, was gradually decreased as the Rh precursor dosage increased (Fig. 4b), due to the reduced activity and the lowered atom utilization efficiency. The influence of optical intensity was also examined. As shown in Fig. 4c, syngas evolution rate exhibits an obvious increasing trend with light intensity. As expected, syngas generation did not occur in the dark under ambient conditions. In sharp contrast, upon introduction of suitable photons, the thermodynamic limit of syngas production from methane and water was broken, leading to an appreciable activity of $0.6\,mol \cdot g_{cat}^{-1} \cdot h^{-1}$ under light illumination of $3.7\,W \cdot cm^{-2}$. Increasing light intensity resulted in a significant promotion on the activity. Specifically, as the light intensity approached to $6.3\,W \cdot cm^{-2}$, the syngas activity reached $6.5\,mol \cdot g_{cat}^{-1} \cdot h^{-1}$ with a
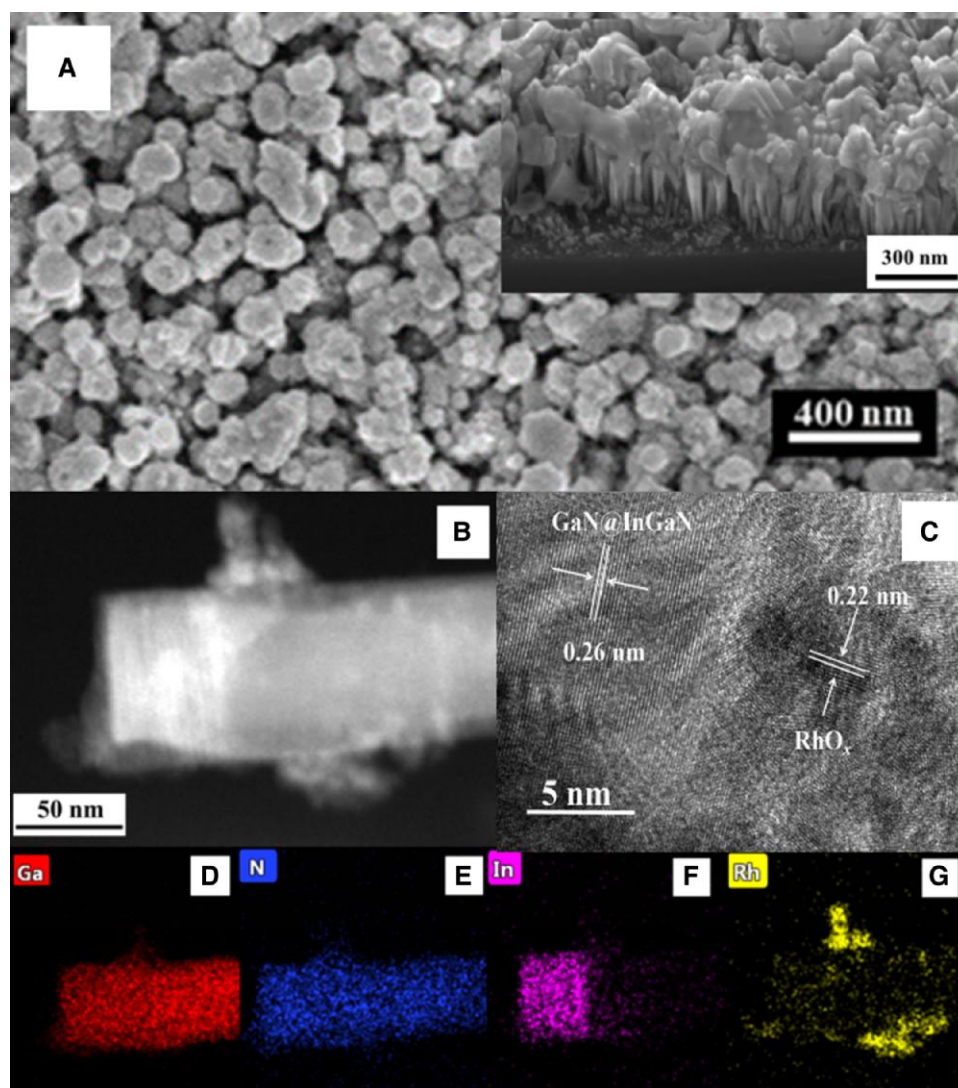
Fig. 2. Characterization of RhO$_x$/GaN@InGaN NWs hybrid. a) Front-view SEM image of RhO$_x$/GaN@InGaN NW hybrid vertically aligned on silicon. b) Scanning transmission electron microscopy images of RhO$_x$/GaN@InGaN NWs at low resolution. c) HRTEM image of RhO$_x$/GaN@InGaN NWs. The elemental mapping images of RhO$_x$/GaN@InGaN NWs: d) Ga, e) N, f) In, and g) Rh.

CO/H$_2$ ratio of 2.3. Under various illuminating condition, as measured by the infrared camera, the surface temperature of RhO$_x$/GaN@InGaN NWs is 238.4, 315.5, 373.9, and 433.7°C, corresponding to under the 3.7, 4.8, 5.7, and 6.3 W·cm^{-2}, respectively (Fig. S12). Under concentrated light illumination, the remarkable photothermal effect was critical for methane steam reforming. As shown in Fig. 4c and Fig. S13, the photothermal activity of syngas far outperforms the pure thermocatalytic activity under the same reaction temperature by external thermal energy without illumination. In particular, the evolution rate of CO and H$_2$ was as low as 0.267 and 0.21 mol·g$_{cat}^{-1}$·h^{-1} at 433.7°C in the dark, which is only about 15.7% of the photothermal activity under 6.3 W·cm^{-2} irradiation without any other energies. These results validate the viability of employing energetic photoexcited carriers and thermal energy to improve methane steam reforming under concentrated light illumination. It is noted that the performance of RhO$_x$/GaN@InGaN NWs far exceeds state-of-the-art catalysts under comparable reaction conditions, exhibiting the superiority of the developed photocatalyst for green syngas production (Table S2). The influence of H$_2$O on the reaction was studied as well (Fig. 4d and Fig. S14). When only a small amount of 1-mL

water was added into the reaction chamber, water was readily evaporated under concentrated light irradiation. Under this condition, RhO$_x$/GaN@InGaN NWs showed a superior syngas evolution rate of 8.1 mol·g$_{cat}^{-1}$·h^{-1}, and H$_2$/CO ratio was estimated to 2.4. The activity of syngas decreased with the increasing amount of water. Especially, by further increasing water to 10 mL, the syngas activity dramatically declined to 2 mol·g$_{cat}^{-1}$·h^{-1} with a H$_2$/CO ratio of 1.2. It is likely attributed to that there exists adsorption competition between methane and water over the interface of RhO$_x$/GaN@InGaN NWs (25). Methane adsorption on the catalytic sites could be inhibited by water molecules at a high dosage of water in the reaction system, thus showing relatively reduced activity. Moreover, control experiments showed that GaN@InGaN NWs and RhO$_x$ played vital roles in the superior performance (Fig. S15). It can be inferred from the extremely low activity of RhO$_x$-decorated GaN thin film supported by sapphire (RhO$_x$/GaN TF/sapphire), which is 2,695 times lower than that of RhO$_x$/GaN@InGaN NWs under the same conditions (Fig. S16). Herein, the unprecedented activity of RhO$_x$/GaN@InGaN NWs is probably attributed to the following three reasons. Firstly, the multistacked GaN@InGaN NWs enabled the spatial decoupling of light
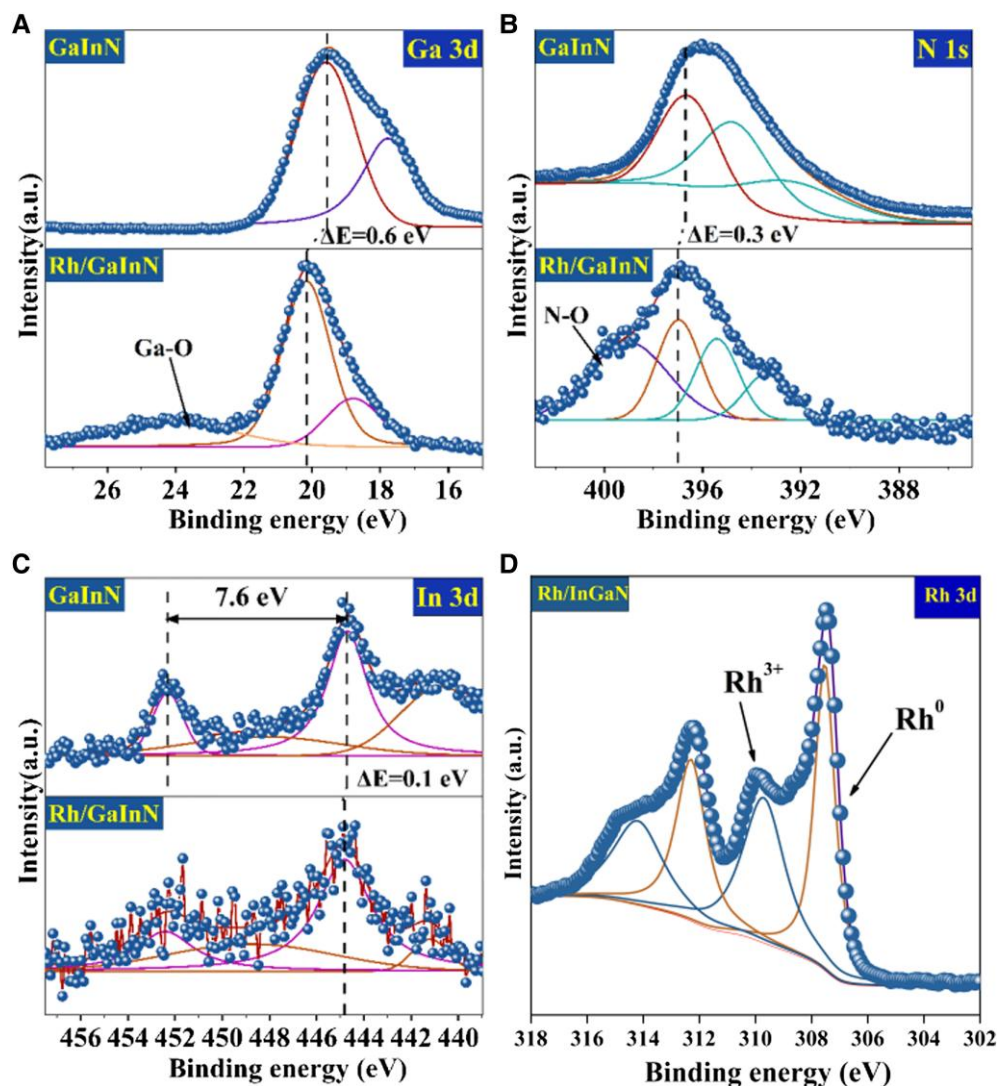
Fig. 3. XPS measurements. High-resolution XPS spectra of a) Ga 3d, b) N 1s, and c) In 3d for GaN@InGaN NWs and RhO_x/GaN@InGaN NWs and d) Rh 3d for RhO_x/GaN@InGaN NWs.

absorption and charges separation. Secondly, 1D geometry of the hybrid is favorable for high accessibility of the reactants to catalytic centers with high-density active sites (16, 17). Most importantly, the unique surface of RhO_x/GaN@InGaN NWs is beneficial for simultaneously activating the two reactants of CH_4 and H_2O despite remarkable geometric and electronic difference, thus resulting in dramatic reduction in energy barrier. What is more, the syngas rate of RhO_x/GaN@InGaN NWs is also superior to that of RhO_x/GaN because the incorporation of indium can enhance light absorption of GaN NWs by narrowing the bandgap (Fig. 4e). These results verify the critical role of GaN@InGaN NWs for the achievement of outstanding performance. Long-term stability test showed that after 300 min of operation, an impressive turnover number of 10,493 mol syngas per mol Rh was achieved without significantly varied TOF, suggesting the decent stability of RhO_x/GaN@InGaN NWs for syngas production from CH_4 and H_2O (Fig. 4f and Fig. S17). The elemental and morphological characterizations showed that RhO_x could be reduced toward metal state (Rh^0) during the reaction, and some of GaN@InGaN NWs fell down. These observations explain the activity degradation after 300 min of stability test (Figs. S18 and S19). Control experiments further indicated that syngas indeed

originated from methane and water by photocatalytic reforming (Fig. S20).

In situ spectroscopy measurements

To better understand the reaction mechanism, in situ spectroscopic investigations were correlatively performed. The in situ XPS was measured to explore the transfer direction of photocarriers in Fig. 5a. It is found that there is a negative shift of Rh 3d spectra under light illumination, indicating that Rh species served as efficient photoexcited electron sinks. It thus facilitates the reaction by not only offering active sites but also promoting the electron-hole separation, in line with PL measurement (Fig. S8). Furthermore, under the illumination, it can not only promote the separation of photocarriers but also act as a extractor of photoelectrons, which is convenient to participate in the C–H and O–H bond cleavage on CH_4 and H_2O molecules, respectively. To tracking the carbon source of the product CO, ^{13}C-labeled CH_4 was employed for methane steam reforming reaction. As detected by the gas chromatography–mass spectrometer, ^{13}CO is clearly shown in Fig. 5b, indicating that the carbon in the product mainly derived from CH_4. By operando electron paramagnetic resonance (EPR)
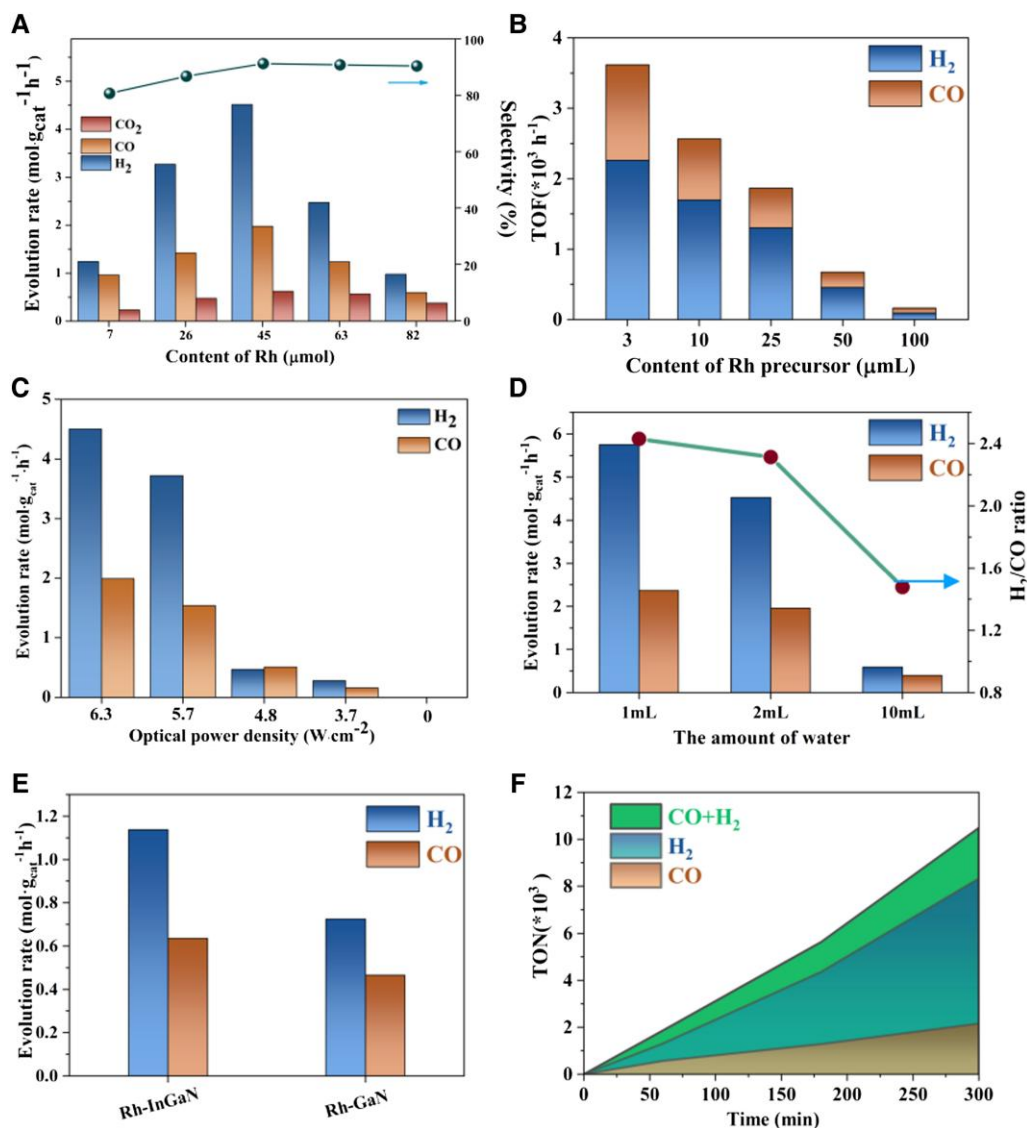
Fig. 4. Syngas evolution from photocatalytic methane steam reforming. Influence of Rh content on activity and syngas selectivity a) and TOF b) of syngas. Influence of optical density c) and water amount d) on the performance. Performance comparison between RhO$_x$/GaN@InGaN NWs and RhO$_x$/GaN NWs. f) Turnover number of CO + H$_2$ over 300 min of stability test. Experimental conditions: 360-mL argon, 40-mL CH$_4$, atmospheric pressure, 300-W Xenon lamp, 6.3 W·cm^{-2}, reaction time 1 h.

characterizations, as shown in Fig. 5c, the characteristic signals of hydroxyl radicals, i.e. •OH, were observed and persistently increased with the illumination time. Herein, •OH species primarily originated from H$_2$O dissociation (27–29). Another key intermediate, i.e. •CH$_3$, was clearly observed as well, validating effective activation of the inert C–H bond in CH$_4$ over RhO$_x$/GaN@InGaN NWs (30). However, if light illumination was removed, both •OH and •CH$_3$ disappeared shortly. The results above validate that the photoexcited charge carriers of GaN@InGaN NWs are essential to initiate the reaction by offering highly active species like •OH and •CH$_3$ from water splitting and methane reforming. To get an in-depth understanding of the process, in situ diffuse reflectance infrared Fourier transform spectroscopy characterization was further conducted to study the evolution of the reactants and/or intermediates. As illustrated in Fig. 5d, a series of characteristic peaks diffuse reflectance infrared Fourier-transform (DRIFT) spectroscopy appeared over RhO$_x$/GaN@InGaN NWs under light irradiation and their intensities varied with the irradiation time. For example, the intensities of the adsorbed water species at

3,636 and 3,608 cm^{-1} decreased with the elongating irradiation time, indicating the gradual depletion of water molecules adsorbed on the catalytic surface for producing syngas as the reaction proceeded (31). Notably, a characteristic band of metal hydroxide species at 3,666 cm^{-1} was observed. It suggested that water was split into hydroxyl and hydrogen, and the formed hydroxyl preferred to sit on Rh species (32). This observation is well consistent with the results of DFT calculations in Fig. 1. Moreover, the typical *CH$_3$ species were observed at the characteristic bands of 3,092, 3,016, 2,824, 1,338, and 1,304 cm^{-1} (33, 34), which came from the homolytic C–H bond cleavage of CH$_4$. It is well matched with the operando EPR measurements. The adsorbed *CH$_3$ species were readily oxidized with *OH toward various intermediates, e.g. HCHO* (2,892, 1,035, and 1,010 cm^{-1}) (35–37), *CO (2,076 cm^{-1}) (38), and HCOO* (1,604 cm^{-1}) (39–42). The critical information above showed a clear evolution profile of methane steam reforming toward syngas over RhO$_x$/GaN@InGaN NWs. Herein, the multifunctional RhO$_x$/GaN interface is efficient for overcoming the remarkable geometric and polar difference
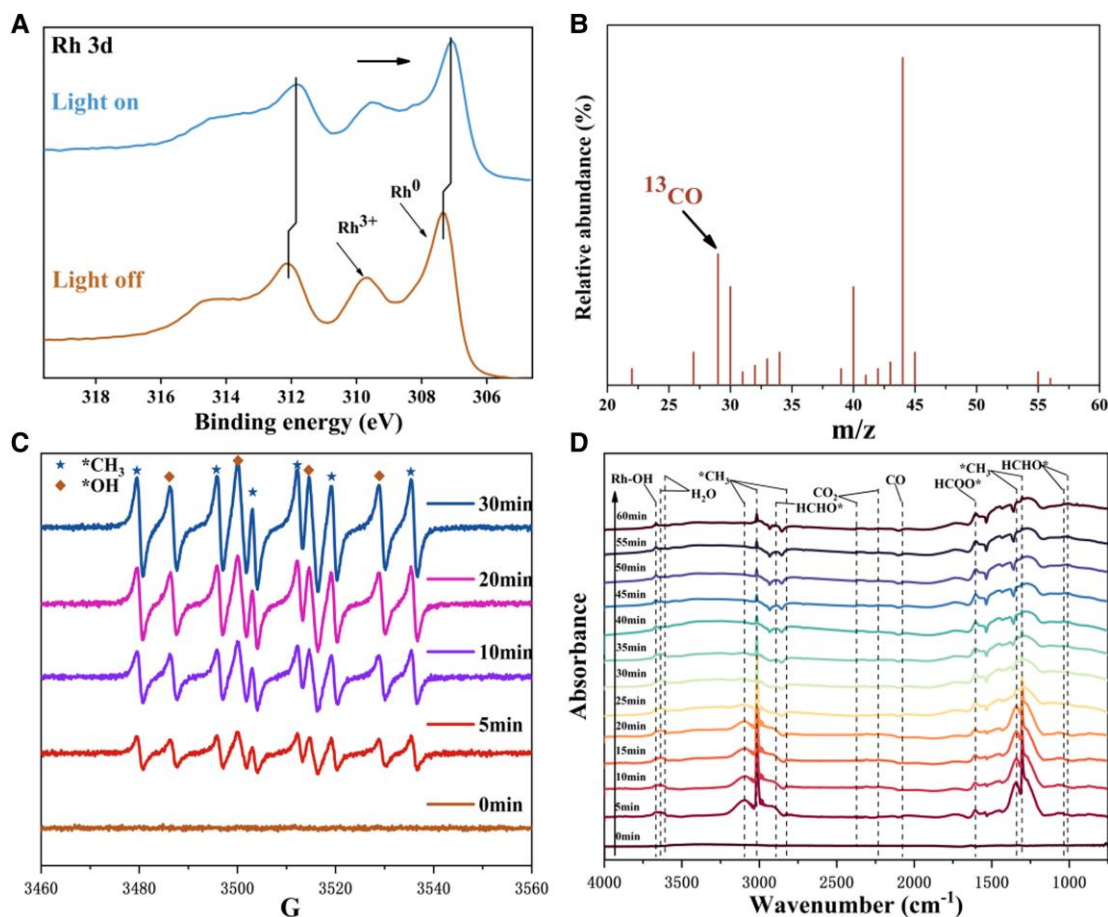
Fig. 5. a) In situ XPS spectra of Rh 3d of RhO_x/GaN@InGaN NWs. b) Gas chromatography–mass spectra of CO produced from ^{13}C-labeled CH_4 and H_2O over RhO_x/GaN@InGaN NWs. Test condition: 300-W Xenon lamp, 6 W·cm^{-2}, [13]CH_4 40 mL, inert gas 360 mL, H_2O 1 mL, 1 h. c) Operando EPR spectroscopy characterizations for studying hydroxyl radicals and methyl radicals during photocatalytic methane steam reforming over RhO_x/GaN@InGaN NWs under experimental conditions. 5,5-Dimethy-l-1-pyrroline N-oxide was employed as the spin trapping agent. d) In situ DRIFT spectra of photocatalytic methane steam reforming under different light irradiation time over RhO_x/GaN@InGaN NWs.

between CH_4 and H_2O with the aid of energetic charge carriers and thermal energy. It thus simultaneously activates the two reactants of CH_4 and H_2O to produce highly active species, e.g. *CH_3 and *OH, leading to exceptional syngas production via an energy-favorable pathway, which will be studied by DFT calculations next.

Density functional theoretical calculations

To reveal the origin of the exceptional performance, 105 possible reaction pathways of methane steam reforming toward syngas were simulated by employing the rationalized Rh_6O_9/GaN model. Three elementary steps for syngas production, i.e. CH_4 dehydrogenation, H_2O dehydrogenation, and CO desorption, were investigated in detail (Fig. S21). Three energetically favored reaction paths are summarized in Fig. 6 as well as the optimized structures of essential intermediates (Fig. S22). It is found that *CH_3-to-*CH_2 dehydrogenation is the potential-determining step of the entire process. Of note, due to the Lewis acid/base pair nature of Rh_6O_9/GaN nanoarchitecture, the generation of CO occurs on Rh_6O_9 cluster while H_2 is preferably produced on GaN surface, which is spatially separated. This facilitates the adequate segregation of photogenerated electrons and holes, thus leading to excellent redox reaction efficiency (43, 44). Additionally, the energy step for *CO-to-CO desorption from Rh_6O_9/GaN system is as small

as 0.19 eV, which greatly favors the escape of CO from the catalytic interface and breezily evades the unnecessary generation of CO_2. These above results are in excellent agreement with the corresponding experimental measurements, providing solid theoretical explanation for the superior activity of the reaction.

Conclusion

In summary, a rational RhO_x/GaN@InGaN NW hybrid has been assembled for syngas generation from photocatalytic methane steam reforming. Both theoretical and experimental investigations showed that the multifunctional interface of RhO_x/GaN was efficient for simultaneously activating CH_4 and H_2O by stretching the C–H and O–H bonds due to Lewis acid/base nature of Rh_6O_9/GaN nanoarchitecture. Upon light illumination, the energetic charges enable the formation of active species, i.e. *H, *OH, and *CH_3, from the absorbed CH_4 and H_2O via water oxidation and C–H cleavage. At the end, CO and H_2 were spatially generated over Rh_6O_9 cluster and GaN surface via energetically favored pathway. A decent syngas production rate of 8.1 mol·g^{-1}·h^{-1} was achieved under concentrated light illumination of 6.3 W·cm^{-2}. H_2/CO ratios can be varied from 0.8 to 2.4 for yielding various downstream products. The hybrid demonstrated a decent high TON of 10,493 mol syngas per mol RhO_x over 300 min of stability test. This work presents a disruptive strategy for breaking
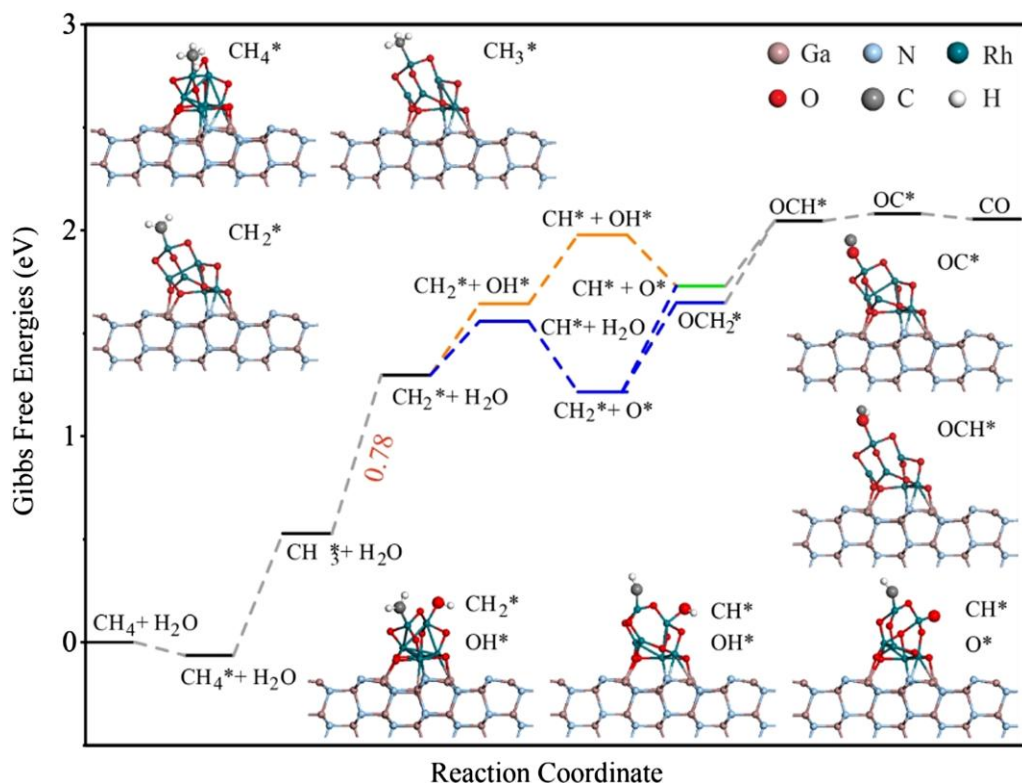
Fig. 6. Potential energy diagram of methane steam reforming reaction. The optimized structures for essential intermediate steps are plotted.

the limit of methane steam reforming toward syngas under ambient conditions with the use of renewable solar energy.

Supplementary Material

Supplementary material is available at *PNAS Nexus* online.

Author Contributions

D.L. performed the research and wrote the paper. Z.W. contributed to the DFT calculations and wrote the paper. Y.L. performed the research, contributed new analytic tools, analyzed data, and wrote the paper. X.F. contributed analyzed data. S.M.H., S.A., and M.R. performed the research. J.L., Z.W., and T.Y. contributed to analyzed the data. X.K. led the computational research, performed DFT calculations, and wrote the paper. L.Z. contributed analyzed the data. S.M.S. performed research. B.Z. designed and led the whole research, analyzed the data, and wrote the paper.

Data Availability

The data underlying this article are available in the article and in its online supplementary material.

References

1   Huang J, Liu, Yang Y, Liu B. 2018. High-performance Ni–Fe redox catalysts for selective CH_4 to syngas conversion via chemical looping. *ACS Catal.* 8:1748–1756.

2   Song H, *et al.* 2018. Visible-light-mediated methane activation for steam methane reforming under mild conditions: a case study of Rh/TiO_2 catalysts. *ACS Catal.* 8:7556–7565.

3   Liu Z, *et al.* 2019. Highly active ceria-supported Ru catalyst for the dry reforming of methane: in situ identification of $Ru^{\delta+}$–Ce^{3+} interactions for enhanced conversion. *ACS Catal.* 9:3349–3359.

4   Han B, Wei W, Li M, Sun K, Hu YH. 2019. A thermo-photo hybrid process for steam reforming of methane: highly efficient visible light photocatalysis. *Chem Comm.* 55:7816–7819.

5   Salcedo A, *et al.* 2021. Reaction pathway for coke-free methane steam reforming on a Ni/CeO_2 catalyst: active sites and the role of metal-support interactions. *ACS Catal.* 11:8327–8337.

6   Schwach P, Pan X, Bao X. 2017. Direct conversion of methane to value-added chemicals over heterogeneous catalysts: challenges and prospects. *Chem Rev.* 117:8497–8520.

7   Ravi M, Ranocchiari M, van Bokhoven JA. 2017. The direct catalytic oxidation of methane to methanol—a critical assessment. *Angew Chem Int Ed.* 56:16464–16483.

8   Gao W, *et al.* 2020. Industrial carbon dioxide capture and utilization: state of the art and future challenges. *Chem Soc Rev.* 49:8584–8686.

9   Che F, Gray JT, Ha S, McEwen J-S. 2016. Improving Ni catalysts using electric fields: a DFT and experimental study of the methane steam reforming reaction. *ACS Catal.* 7:551–562.

10 Olivos-Suarez AI, *et al.* 2016. Strategies for the direct catalytic valorization of methane using heterogeneous catalysis: challenges and opportunities. *ACS Catal.* 6:2965–2981.

11 Li X, Wang C, Tang J. 2022. Methane transformation by photocatalysis. *Nat Rev Mater.* 7:617–632.

12 Huang X, Zhao B, Bachirou Guene L, Zhang H, Liu H. 2022. Research progress of methane steam reforming for hydrogen production. *Chem Eng Oil Gas.* 51:53–61.

13 Cho YH, Yamaguchi A, Miyauchi M. 2021. Photocatalytic methane reforming: recent advances. *Catalysts.* 11:18.

14 Iulianelli A, Liguori S, Wilcox J, Basile A. 2016. Advances on methane steam reforming to produce hydrogen through membrane reactors technology: a review. *Catal Rev.* 58:1–35.

15 Zhou B, *et al.* 2018. Gallium nitride nanowire as a linker of molybdenum sulfides and silicon for photoelectrocatalytic water splitting. *Nat Commun.* 9:3856.

16 Cesar M, Ke YQ, Ji W, Guo H, Mi ZT. 2011. Band gap of $In_xGa_{1-x}N$: a first principles analysis. *Appl Phys Lett.* 98:20.

17 Zhou B, Sun S. 2023. Approaching the commercial threshold of solar water splitting toward hydrogen by III-nitrides nanowires. *Front Energy.* https://doi.org/10.1007/s11708-023-0870-z

18 Li Y, Sadaf SM, Zhou B. 2023. Ga(X)N/Si nanoarchitecture: an emerging semiconductor platform for sunlight-powered water splitting toward hydrogen. *Front Energy.* https://doi.org/10.1007/s11708-023-0881-9

19 Liu D, *et al.* 2015. The nature of photocatalytic "water splitting" on silicon nanowires. *Angew Chem Int Ed.* 54:2980–2985.

20 Shi H, *et al.* 2014. Polymeric $g-C_3N_4$ coupled with $NaNbO_3$ nanowires toward enhanced photocatalytic reduction of CO_2 into renewable fuel. *ACS Catal.* 4:3637–3643.

21 Wang R, Xu HY, Liu XB, Ge QJ, Li WZ. 2006. Role of redox couples of $Rh^0/Rh^{\delta+}$ and Ce^{4+}/Ce^{3+} in CH_4/CO_2 reforming over $Rh-CeO_2/Al_2O_3$ catalyst. *APPL CATAL A-GEN.* 305:204–210.

22 Rashid RT, *et al.* 2022. Tunable green syngas generation from CO_2 and H_2O with sunlight as the only energy input. *Proc Natl Acad Sci U S A.* 119:e2121174119.

23 Kundu MK, Mishra R, Bhowmik T, Barman S. 2018. Rhodium metal–rhodium oxide ($Rh-Rh_2O_3$) nanostructures with Pt-like or better activity towards hydrogen evolution and oxidation reactions (HER, HOR) in acid and base: correlating its HOR/HER activity with hydrogen binding energy and oxophilicity of the catalyst. *J Mater Chem A.* 6:23531–23541.

24 Li JL, *et al.* 2022. Oxynitride-surface engineering of rhodium-decorated gallium nitride for efficient thermocatalytic hydrogenation of carbon dioxide to carbon monoxide. *Commun Chem.* 5:107.

25 Pan Y, Zhang C, Liu Z, Chen C, Li YD. 2020. Structural regulation with atomic-level precision: from single-atomic site to diatomic and atomic interface catalysis. *Matter.* 2:78–110.

26 Li GQ, *et al.* 2016. All the catalytic active sites of MoS_2 for hydrogen evolution. *J Am Chem Soc.* 138:16632–16638.

27 Han SK, Nam SN, Kang JW. 2002. OH radical monitoring technologies for AOP advanced oxidation process. *Water Sci Technol.* 46:7–12.

28 Pan X, Chen S, Yan X, Dong W, Hou H. 1999. Determination of gas-phase OH radical concentrations using electron paramagnetic resonance. *J Environ Sci (China).* 20:30–33.

29 Taira J, *et al.* 1993. Effective inhibition of hydroxyl radicals by hydroxylated biphenyl compounds. *Free Radic Res.* 19:S71–S77.

30 Li GX, Luo ZY, Wang WB, Cen JM. 2020. A study of the mechanisms of guaiacol pyrolysis based on free radicals detection technology. *Catalysts.* 10:295.

31 Liu ZY, *et al.* 2018. Methanol steam reforming over $Ni-CeO_2$ model and powder catalysts: pathways to high stability and selectivity for H_2/CO_2 production. *Catal Today.* 311:74–80.

32 Awbery RP, Broughton DA, Tsang SC. 2008. In situ observation of lithium hydride hydrolysis by DRIFT spectroscopy. *J Nucl Mater.* 373:94–102.

33 Vogt C, *et al.* 2018. Unravelling structure sensitivity in CO_2 hydrogenation over nickel. *Nat Catal.* 1:127–134.

34 Schadle T, Pejcic B, Mizaikoff B. 2016. Monitoring dissolved carbon dioxide and methane in brine environments at high pressure using IR-ATR spectroscopy. *Anal Methods.* 8:756–762.

35 Chiarello GL, Ferri D, Selli E. 2018. In situ attenuated total reflection infrared spectroscopy study of the photocatalytic steam reforming of methanol on Pt/TiO_2. *Appl Surf Sci.* 450:146–154.

36 Li H, Li J, Ai ZH, Jia FL, Zhang LZ. 2018. Oxygen vacancy-mediated photocatalysis of BiOCl: reactivity, selectivity, and perspectives. *Angew Chem Int Ed.* 57:122–138.

37 Hayyan M, Hashim MA, AlNashef IM. 2016. Superoxide ion: generation and chemical implications. *Chem Rev.* 116:3029–3085.

38 Luo S, *et al.* 2021. Triggering water and methanol activation for solar-driven H_2 production: interplay of dual active sites over plasmonic ZnCu alloy. *J Am Chem Soc.* 143:12145–12153.

39 Rasko J, Kecskes T, Kiss J. 2004. Formaldehyde formation in the interaction of HCOOH with Pt supported on TiO_2. *J Catal.* 224:261–268.

40 Nomikos GN, Panagiotopoulou P, Kondarides DI, Verykios XE. 2014. Kinetic and mechanistic study of the photocatalytic reforming of methanol over Pt/TiO_2 catalyst. *Appl Catal B.* 146:249–257.

41 Kecskes T, Rasko J, Kiss J. 2004. FTIR and mass spectrometric studies on the interaction of formaldehyde with TiO_2 supported Pt and Au catalysts. *Appl Catal A-Gen.* 273:55–62.

42 Chen ZM, Wang CX. 2006. Rate constants of the gas-phase reactions of CH_3OOH with O_3 and NO_x at 293 K. *Chem Phys Lett.* 424:233–238.

43 Nyathi TM, *et al.* 2019. Impact of nanoparticle-support interactions in Co_3O_4/Al_2O_3 catalysts for the preferential oxidation of carbon monoxide. *ACS Catal.* 9:7166–7178.

44 Gausemel I, Ellestad OH, Nielsen CJ. 1997. On the use of infrared spectroscopy in the study of carbon dioxide decomposition on copper containing methanol synthesis catalysts. *Catal Lett.* 45:129–133.